Received: 7 January 2022 | Revised: 8 June 2022 | Accepted: 9 June 2022 | Published on: 4 July 2022

DOI: 10.1002/mrm.29375

RESEARCH ARTICLE

Magnetic Resonance in Medicine

A workflow for predicting temperature increase at the electrical contacts of deep brain stimulation electrodes undergoing MRI

Alireza Sadeghi-Tarakameh[1] | Nur Izzati Huda Zulkarnain[1] | Xiaoxuan He[1] | Ergin Atalar[2,3] | Noam Harel[1] | Yigitcan Eryaman[1]

[1]Center for Magnetic Resonance Research (CMRR), University of Minnesota, Minneapolis, Minnesota USA

[2]Department of Electrical and Electronics Engineering, Bilkent University, Ankara, Turkey

[3]National Magnetic Resonance Research Center (UMRAM), Bilkent University, Ankara, Turkey

Correspondence
Alireza Sadeghi-Tarakameh, Center for Magnetic Resonance Research (CMRR), University of Minnesota, 2021 6th Street Southeast, Minneapolis, MN 55455, USA.
Email: sadeg032@umn.edu

Funding information
National Institute of Biomedical Imaging and Bioengineering, Grant/Award Number: P41 EB027061; National Institute of Neurological Disorders and Stroke, Grant/Award Number: R01NS115180

Purpose: The purpose of this study is to present a workflow for predicting the radiofrequency (RF) heating around the contacts of a deep brain stimulation (DBS) lead during an MRI scan.

Methods: The induced RF current on the DBS lead accumulates electric charge on the metallic contacts, which may cause a high local specific absorption rate (SAR), and therefore, heating. The accumulated charge was modeled by imposing a voltage boundary condition on the contacts in a quasi-static electromagnetic (EM) simulation allowing thermal simulations to be performed with the resulting SAR distributions. Estimating SAR and temperature increases from a lead in vivo through EM simulation is not practical given anatomic differences and variations in lead geometry. To overcome this limitation, a new parameter, transimpedance, was defined to characterize a given lead. By combining the transimpedance, which can be measured in a single calibration scan, along with MR-based current measurements of the lead in a unique orientation and anatomy, local heating can be estimated. Heating determined with this approach was compared with results from heating studies of a commercial DBS electrode in a gel phantom with different lead configurations to validate the proposed method.

Results: Using data from a single calibration experiment, the transimpedance of a commercial DBS electrode (directional lead, Infinity DBS system, Abbott Laboratories, Chicago, IL) was determined to be 88 Ω. Heating predictions using the DBS transimpedance and rapidly acquired MR-based current measurements in 26 different lead configurations resulted in a <23% (on average 11.3%) normalized root-mean-square error compared to experimental heating measurements during RF scans.

This is an open access article under the terms of the Creative Commons Attribution-NonCommercial-NoDerivs License, which permits use and distribution in any medium, provided the original work is properly cited, the use is non-commercial and no modifications or adaptations are made.
© 2022 The Authors. *Magnetic Resonance in Medicine* published by Wiley Periodicals LLC on behalf of International Society for Magnetic Resonance in Medicine.

Conclusion: In this study, a workflow consisting of an MR-based current measurement on the DBS lead and simple quasi-static EM/thermal simulations to predict the temperature increase around a DBS electrode undergoing an MRI scan is proposed and validated using a commercial DBS electrode.

KEYWORDS
deep brain stimulation safety, MRI, radiofrequency heating, temperature prediction

1 | INTRODUCTION

Deep brain stimulation (DBS) is a powerful therapeutic approach that improves the lives of patients who have Parkinson's disease, essential tremor, and dystonia.[1–6] These patients, because of their existing conditions, are far more likely to need an MR scan than the healthy population. However, MRI scans performed in the presence of DBS electrodes can pose significant risks to the patients. Radiofrequency (RF) coils can induce currents on elongated metallic leads, which may critically increase the temperature at the lead tip[7] and potentially cause irreversible damage to the surrounding tissue.[8] Therefore, it is critical to assess the risk of RF heating before scanning patients with DBS systems.

Various approaches have been proposed for predicting the temperature increase at the tip of metallic implants. For example, full-wave electromagnetic (EM) simulations have been performed using the model of the RF coil, the electrode, and realistic human models.[9–15] Although this approach is valuable for gaining insight into different factors that affect the heating (e.g., electrode trajectory, the effect of implantable pulse generator [IPG]), it usually requires high computational power and expertise. Even with the availability of both, it is still challenging and time consuming to simulate the full model of a DBS electrode because of the complexity of the conductor geometry and the fine mesh size (~microns) required.

Other approaches have been proposed to tackle the complexities of full-wave EM simulation of metallic implants. For example, Acikel et al[16] proposed the modified transmission line method (MoTLiM) to model a metallic wire within a lossy medium, mimicking an implantable lead inside human tissue, using a distributed impedance along with an effective wavenumber. Using this approach, the induced RF current on a wire exposed to a known electric field inside a uniform lossy medium was successfully predicted. Nevertheless, calculating the modeling parameters (i.e., the impedance and wavenumber) can be challenging for realistic DBS electrodes in a non-uniform human model. Moreover, the incident electric field along an electrode with a complex trajectory is not known in advance. Therefore, EM simulations involving the RF coil as well as the patient-specific model need to be performed. In another study, Park et al[17] introduced the transfer function (TF) relating the incident tangential electric field to the scattered electric field at the tip of the implant. The TF was determined by measuring the response of an implant to piece-wise localized electric field exposures using dedicated bench set-ups.[18] However, this approach needs precise positioning of an electric-field probe at the tip of the electrode and a continuous movement of a transmitter along the lead trajectory, which is not possible to perform in vivo. Tokaya et al[19,20] introduced the transfer matrix (TM) concept and presented an MR-based measurement technique to determine the TM corresponding to the lead undergoing an MRI scan. The TM extends the TF concept and relates the incident tangential electric field to the current distribution on the implant. It also characterizes the RF response along the entire implant. One major limitation of the TM technique is that in the case of highly-elongated implants, corresponding MR-based measurement requires increasing field of view of the MRI scanner beyond the range of acceptable and reliable gradient performance. A general challenge for the TF/TM method is the necessity for a detailed EM simulation of the patient within the RF coil to determine the tangential electric field, whereas this model (i.e., either the coil or the subject or both) is not usually available.

In addition to the modeling efforts summarized above, hardware-based solutions have also been proposed in the literature. For example, Silemek et al[21] proposed adding a temperature sensor to the electrode, which allowed patient-specific real-time temperature monitoring at the tissue contacts. Although high accuracy was demonstrated in temperature measurement, this approach required a hardware modification on the electrode, which may not always be desirable from the vendors' perspective because of the design and manufacturing challenges as well as a long and complicated the United States Food and Drug

Administration approval process. Furthermore, such modifications would most likely be not feasible for patients who were already implanted with conventional DBS electrodes.

Considering all the approaches summarized above, patient-specific safety assessment is still an unmet medical need for patients with DBS electrodes. In this work, a workflow is proposed for predicting RF heating at the contact points of commercial DBS electrodes using the previously proposed MR-based current measurement method.[22] It is hypothesized that the current flowing on the shaft (near the tip) is linearly proportional to the charge density on the contact (consequently, the voltage). The ratio between the contact voltage and shaft current is defined as an equivalent transimpedance and assumed to be independent of the electrode trajectory as well as its length and termination at the distal end (i.e., IPG). This assumption was validated for a commercial DBS electrode (directional lead, Infinity DBS system, Abbott Laboratories, Chicago, IL) with experiments conducted with various electrode trajectories and terminations, measuring the temperature at different radial distances from the multiple contacts of the electrode.

2 | THEORY

Previously, it has been shown that the induced current, I_{ind}, by an RF coil on a DBS electrode aligned in the z-direction (Figure 1A) can be related to the incident

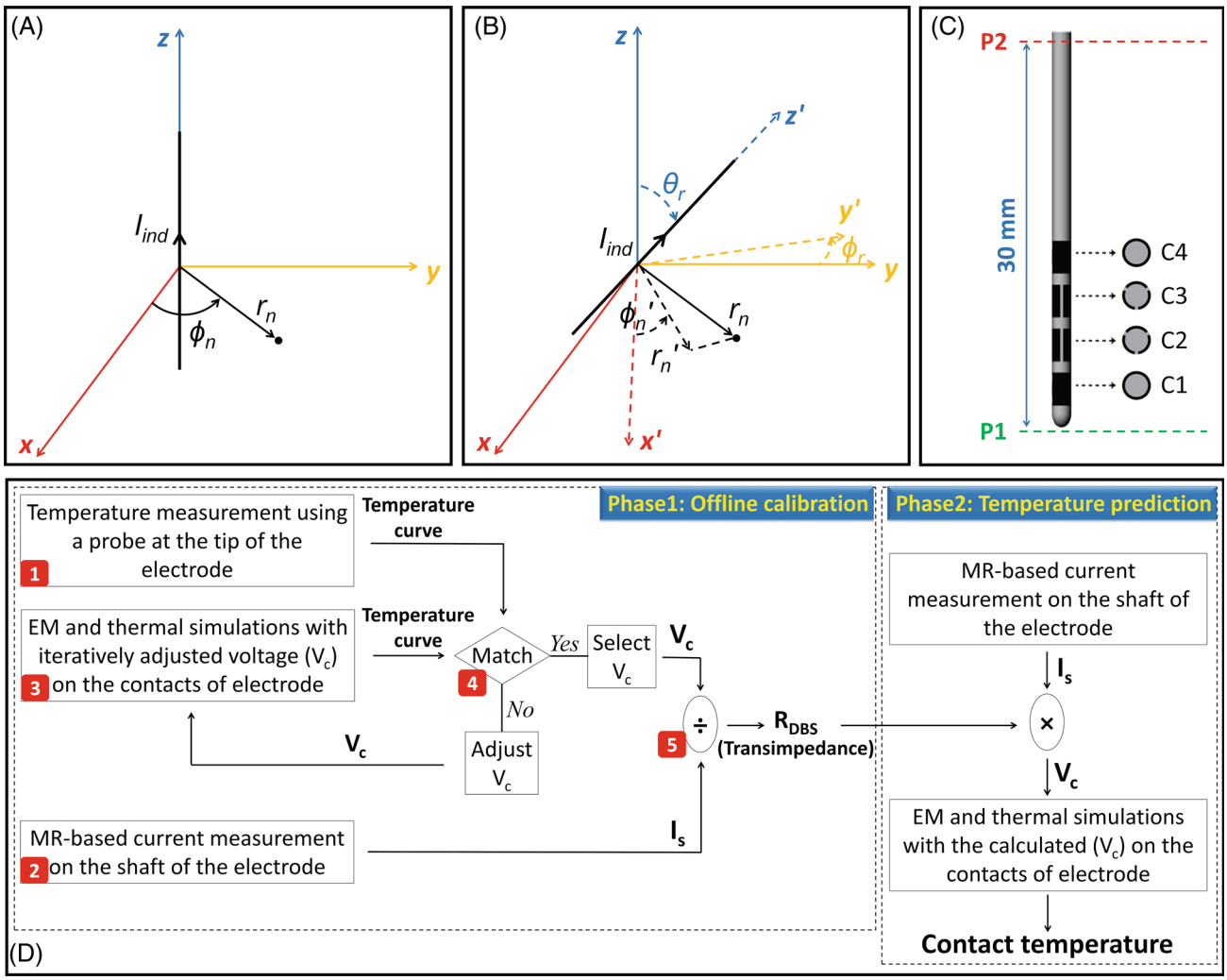

FIGURE 1 Deep brain stimulation (DBS) electrode orientation and configuration. Induced current on a DBS electrode (A) perpendicular to the transverse plane (aligned in the z-direction), and (B) oblique to the transverse plane. (C) Configuration of the B_1 mapping plane (P1), shaft current measurement plane (P2), and contacts of the commercial DBS electrode. (D) Workflow for predicting RF heating at the contact points of commercial DBS electrodes because of RF exposure in MRI. Phase 1: offline calibration to determine the transimpedance, R_{DBS}. Phase 2: Temperature prediction

magnetic field as follows.[22]

$$I_{\text{ind}} = \frac{4\pi r_{\text{n}} \left| B1^{+}_{\text{inc}} \right|}{\mu_0} e^{j\phi_{\text{n}}}, \tag{1}$$

where, $B1^{+}_{\text{inc}}$ is the left-handed circularly-polarized component of the incident transmit magnetic field produced by the RF coil around the electrode, r_{n} is the radial distance of the Tx-null (defined by Eryaman et al)[22] from the electrode, and ϕ_{n} denotes the azimuthal angle of the Tx-null's location in the conventional MRI scanner coordinate system (i.e., laboratory frame). Because DBS electrodes usually have oblique orientations, a general formulation is needed for realistic electrode trajectories. For this purpose, a secondary cylindrical coordinate (r', ϕ', z') system was defined whose z-axis is aligned with the oblique electrode. As shown in Figure 1B, this coordinate system is rotated by a polar angle, θ_{r}, and an azimuthal angle, ϕ_{r}, with respect to the primary coordinate system (r, ϕ, z). Considering this configuration, the magnetic field at the null's location generated by the induced current on an oblique lead, I_{ind}, can be presented as follows:

$$\overline{B}_{\text{lead}}\left(r'_{\text{n}}, \phi'_{\text{n}}\right) = \frac{\mu_0 I_{\text{ind}}}{2\pi r_{\text{n}} \cos\theta_{\text{r}}} \hat{\phi}'. \tag{2}$$

The equivalent primary and secondary Cartesian coordinate systems can be related to each other using the rotation matrices as follows:

$$\begin{bmatrix} \hat{x}' \\ \hat{y}' \\ \hat{z}' \end{bmatrix} = R_y(-\theta_r) R_z(-\phi_r) \begin{bmatrix} \hat{x} \\ \hat{y} \\ \hat{z} \end{bmatrix} = \begin{bmatrix} \cos\theta_r \cos\phi_r & \cos\theta_r \sin\phi_r & -\sin\theta_r \\ -\sin\phi_r & \cos\phi_r & 0 \\ \sin\theta_r \cos\phi_r & -\sin\theta_r \sin\phi_r & \cos\theta_r \end{bmatrix} \begin{bmatrix} \hat{x} \\ \hat{y} \\ \hat{z} \end{bmatrix}. \tag{3}$$

Furthermore, the secondary azimuthal unit vector in Equation (2) can be transformed to the Cartesian using the following relation,

$$\hat{\phi}' = -\hat{x}' \sin\phi'_{\text{n}} + \hat{y}' \cos\phi'_{\text{n}}, \tag{4}$$

where

$$\sin\phi'_{\text{n}} = \frac{y'_{\text{n}}}{\sqrt{x'^2_{\text{n}} + y'^2_{\text{n}}}} = \frac{\sin(\phi_{\text{n}} - \phi_{\text{r}})}{\sqrt{\cos^2\theta_{\text{r}}\cos^2(\phi_{\text{n}} - \phi_{\text{r}}) + \sin^2(\phi_{\text{n}} - \phi_{\text{r}})}}, \tag{5}$$

and

$$\cos\phi'_{\text{n}} = \frac{x'_{\text{n}}}{\sqrt{x'^2_{\text{n}} + y'^2_{\text{n}}}} = \frac{\cos\theta_{\text{r}}\cos(\phi_{\text{n}} - \phi_{\text{r}})}{\sqrt{\cos^2\theta_{\text{r}}\cos^2(\phi_{\text{n}} - \phi_{\text{r}}) + \sin^2(\phi_{\text{n}} - \phi_{\text{r}})}}. \tag{6}$$

Substituting corresponding values from Equations (3-6) into Equation (2) and taking the transverse component of the magnetic field (i.e., it is the only component that contributes to the MRI signal) result in the following:

$$\begin{aligned} \overline{B}^{\text{tra}}_{\text{lead}}(r_{\text{n}}, \phi_{\text{n}}) = {} & \frac{\mu_0 I_{\text{ind}}}{2\pi r_{\text{n}} \cos\theta_{\text{r}} \sqrt{\cos^2\theta_{\text{r}}\cos^2(\phi_{\text{n}} - \phi_{\text{r}}) + \sin^2(\phi_{\text{n}} - \phi_{\text{r}})}} \\ & \times \left\{ -\left[\cos\phi_{\text{r}} \sin(\phi_{\text{n}} - \phi_{\text{r}}) + \sin\phi_{\text{r}} \cos(\phi_{\text{n}} - \phi_{\text{r}})\right] \hat{x} \right. \\ & \left. + \left[-\sin\phi_{\text{r}} \sin(\phi_{\text{n}} - \phi_{\text{r}}) + \cos\phi_{\text{r}} \cos(\phi_{\text{n}} - \phi_{\text{r}})\right] \hat{y} \right\} \cos\theta_{\text{r}}. \end{aligned} \tag{7}$$

Elaborating Equation (7) using some basic trigonometric identities lead to the following:

$$\begin{aligned} \overline{B}^{\text{tra}}_{\text{lead}}(r_{\text{n}}, \phi_{\text{n}}) = {} & \frac{\mu_0 I_{\text{ind}}}{2\pi r_{\text{n}} \sqrt{\cos^2\theta_{\text{r}}\cos^2(\phi_{\text{n}} - \phi_{\text{r}}) + \sin^2(\phi_{\text{n}} - \phi_{\text{r}})}} \\ & \left(-\sin\phi_{\text{n}} \hat{x} + \cos\phi_{\text{n}} \hat{y}\right) \\ = {} & \frac{\mu_0 I_{\text{ind}}}{2\pi r_{\text{n}} \sqrt{\cos^2\theta_{\text{r}}\cos^2(\phi_{\text{n}} - \phi_{\text{r}}) + \sin^2(\phi_{\text{n}} - \phi_{\text{r}})}} \hat{\phi}. \end{aligned} \tag{8}$$

Because the r-component of this transverse magnetic field is 0, the corresponding left-handed circularly-polarized magnetic field ($B_1{}^{+}$) can be written in terms of the ϕ-component in the following form.[23,24]

$$B1^{+}_{\text{lead}}(r_{\text{n}}, \phi_{\text{n}}) = \frac{(j\cos\phi_{\text{n}} - \sin\phi_{\text{n}})}{2} \cdot B^{\text{tra}}_{\text{lead},\phi}(r_{\text{n}}, \phi_{\text{n}}). \tag{9}$$

Given the fact that the incident $B_1{}^{+}$ field ($B1^{+}_{\text{inc}}$) and the $B_1{}^{+}$ field scattered by the lead ($B1^{+}_{\text{lead}}$) cancel each other at the location of the null, the magnitude of the shaft current can be written in terms of the incident $B_1{}^{+}$ as follows

$$|I_{\text{ind}}| = \frac{4\pi r_{\text{n}}}{\mu_0} \sqrt{\cos^2\theta_{\text{r}}\cos^2(\phi_{\text{n}} - \phi_{\text{r}}) + \sin^2(\phi_{\text{n}} - \phi_{\text{r}})} \left| B1^{+}_{\text{inc}} \right|. \tag{10}$$

Consequently, at the boundary of the electrode contacts where discontinuity in the conductor occurs, the induced current accumulates electric charge according to Maxwell's continuity equation,

$$\nabla . \overline{J} = -j\omega\rho_{\text{e}}, \tag{11}$$

where ω is the angular Larmor frequency, and $\bar{J}$ and ρ_e denote the electric current and charge densities, respectively. The accumulated electric charge produces the electric field responsible for the DBS heating at the contact points. Elaborating this statement, the power density at location $\bar{r}$ and time t deposited in the surrounding tissues by this electric field can be presented as the specific absorption rate (SAR) as follows.

$$SAR(\bar{r},t)=\frac{\sigma(r)|E(\bar{r},t)|^2}{\rho_m(\bar{r})}, \tag{12}$$

where E is amplitude of the electric field, and σ and ρ_m denote the conductivity and mass density of the surrounding tissues, respectively. Eventually, for a given SAR distribution, the position- and time-dependent tissue temperature, $T(\bar{r},t)$, is governed by Pennes' bioheat equation[25] as follows

$$\begin{aligned}\rho_m(\bar{r})c_p\tfrac{\partial T(\bar{r},t)}{\partial t}-\kappa\nabla^2T(\bar{r},t)+\mu_t(\bar{r},t)\left(T(\bar{r},t)-T_b\right)\\=\rho_m(\bar{r})SAR(\bar{r},t)+Q_m(\bar{r},t),\end{aligned} \tag{13}$$

where c_p, κ, and μ_t represent heat capacity, thermal conductivity, and perfusion constant of the surrounding tissues, respectively. T_b is the blood temperature and $Q_m(\bar{r},t)$ is the power density deposited in the tissue because of the metabolic heat generation. In a uniform phantom experiment where the perfusion and metabolic heat generation are absent, Equation (13) can be rewritten as

$$\rho_m c_p\frac{\partial T(\bar{r},t)}{\partial t}-\kappa\nabla^2T(\bar{r},t)=\rho_m SAR(\bar{r},t). \tag{14}$$

3 | METHODS

The induced current on the shaft (Figure 1C) of a commercial DBS electrode (directional lead, Infinity DBS system, Abbott Laboratories) was calculated using an MR-based measurement along with Equation (10) and defined it as the shaft current, I_s (see Section 3.3 for MR-based current measurement's details).

It is known that if the physical dimension that characterizes a system is much shorter than the EM wavelength at the operating frequency, the quasi-static assumption holds for the system with negligible error. Accordingly, the DBS contacts (~1 mm), as well as the SAR's hot-spot around the tip of the electrode (i.e., a few millimeters), can be assumed to be much smaller than the wavelength (~270-315 mm) inside the human body (with relative permittivity in the range of 60-80) at 123 MHz (the Larmor frequency at 3 T). Therefore, the quasi-static assumption holds, and the accumulated surface charge density on the contacts' surface is associated with an electric potential on the conductive contacts. The difference between this electric potential and the 0-potential at infinity is referred to as the contact voltage, V_c.

Relating the shaft current to the contact voltage, we introduce and define the $DBS_{transimpedance}$, R_{DBS}:

$$R_{DBS}=\frac{V_c}{I_s}. \tag{15}$$

The DBS transimpedance depends only on the electrode geometry and EM properties of the surrounding medium. It is independent of the trajectory of the electrode, incident electric field, and DBS termination (e.g., an IPG), whereas V_c and I_s depend on all of the parameters above.

3.1 | Temperature prediction workflow

A temperature prediction workflow is proposed (see Figure 1D) that consists of 2 phases; offline calibration and temperature prediction. Both phases include an MR-based current measurement (see Section 3.3), a simple quasi-static EM simulation (see Section 3.4), and a transient thermal simulation (see Section 3.5).

In the calibration phase, transimpedance, R_{DBS}, of the DBS electrode is calculated using data acquired with an arbitrary trajectory in a uniform gel phantom (14 g/L Hydroxyethyl Cellulose, 2.25 g/L NaCl, and 0.25 g/L $CuSO_4$ with electrical properties of $\varepsilon_r=79$ and $\sigma=0.45$ S/m) without IPG (see Figure 2A). For this purpose, the following 5 steps were followed.

1. First, an MR heating study is performed to measure temperature-rise at the tip of the electrode using a fiber optic temperature probe (Lumasense Technologies, Santa Clara, CA).
2. The induced shaft current, I_s, on the DBS electrode using an MR-based measurement is calculated.
3. Later, the accumulated charges on the electrode contacts with an arbitrary voltage boundary condition, V_c, on 4 conductive cylinders using an EM simulator are modeled (Sim4Life version 6.0, Zurich Medtech, Zurich, Switzerland). The SAR distribution of this EM simulation is used in a transient thermal solver (Sim4Life version 6.0, Zurich Medtech) to solve the bioheat equation numerically.
4. The voltage boundary condition, V_c, is iteratively adjusted to fit the time course of the temperature rise calculated by the numerical solver to the experimentally measured temperature.

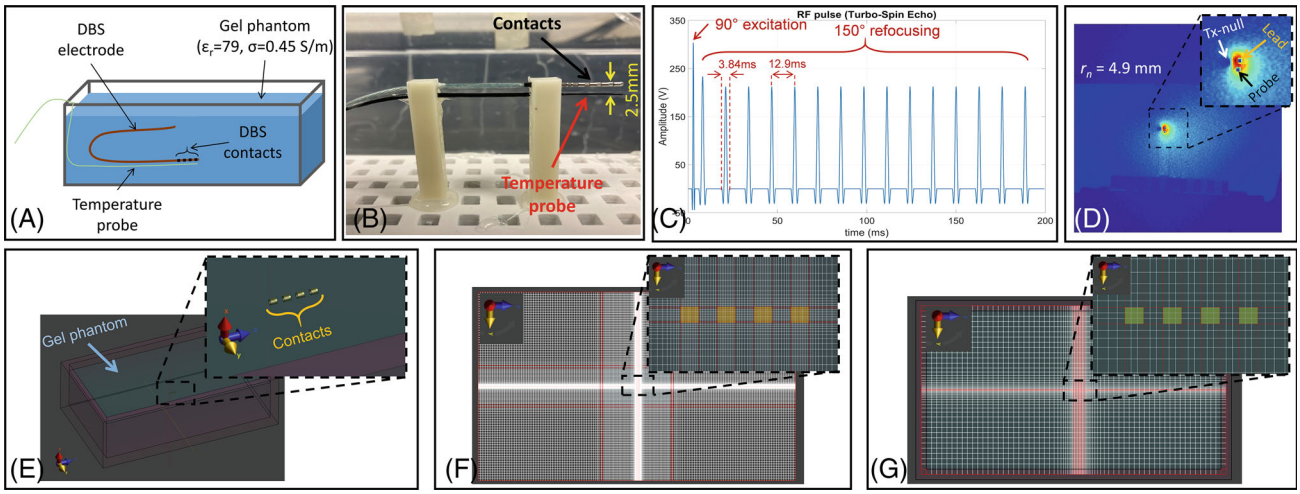

FIGURE 2 Experimental set-up and simulation model for calculating the transimpedance, R_{DBS}, of the deep brain stimulation (DBS) electrode. (A) Demonstration of the DBS electrode and temperature probe immersed into a uniform gel phantom. (B) Arrangement of the electrode and temperature probe to measure the temperature increase around the contact C1. (C) The RF waveform corresponding to the turbo-spin echo (TSE) pulse sequence used in the heating study. (D) Observation of the Tx-null, electrode, and temperature probe in the calibration study using a gradient-echo (GRE) pulse sequence with FA = 5°, repetition time (TR)/TE = 20 ms/2.64 ms, in-plane resolution = 0.5 mm, slice thickness = 3 mm, acquisition matrix = 320 × 320, no. of averages = 1, and pixel bandwidth = 355 Hz/pixel. (E) The DBS electrode contacts were modeled as 4 conductive cylinders in electromagnetic (EM)/thermal simulations. (F) Discretization of the model in the EM simulation. The "extremely fine" mesh setting was used on the contacts, whereas the "fine" mesh setting was used for the rest of the model. (G) Discretization of the model in the thermal simulation. The "fine" mesh setting was used for the entire volume

5. Once a good match is obtained between the numeric and experimental temperature curves, the contact voltage V_c and shaft current I_s in Equation (15) is used to calculate the DBS transimpedance R_{DBS}.

In the second phase, the shaft current was calculated for arbitrary trajectories and termination. The transimpedance, calculated in the calibration phase, was used along with this shaft current to determine the contact voltage. Finally, the calculated contact voltage was imported to the EM/thermal simulation model to predict the time course of the temperature rise.

3.2 | Temperature measurement

All MR experiments in this study were conducted at a 3 T scanner (MAGNETOM Prisma, Siemens Healthineers, Erlangen, Germany) using the conventional dual-drive body coil as the transmitter and a 20-channel head/-neck coil (Head/Neck 20, Siemens Healthineers) as the receiver. All temperature measurements were performed using fiber optic temperature probes during high-power 3D turbo-spin echo (TSE) scans. The temperature data was acquired with a 0.5 s temporal resolution.

In the calibration phase, a TSE pulse sequence was used with FA = 150°, TR/TE = 300 ms/103 ms, in-plane resolution = 0.5 mm, slice thickness = 1.25 mm, acquisition matrix = 512 × 512, TSE-factor 15, no. of averages = 1, and pixel bandwidth = 220 Hz/pixel to heat the implant with quadrature excitation of the body coil (total average input power of 20 W). As shown in Figure 2B, a temperature probe was placed carefully around the contact C1 of the electrode at a distance of 2.5 mm.

3.3 | Current measurement

In this study, it was assumed that the mean value of the incident B_1^+ (around the shaft on plane P2 where the current is measured) is approximately equal to the mean value of total B_1^+ underneath the tip of the electrode on plane P1 (Figure 1C). This approximation is based on the rationale that the lead current has almost 0 impact on the B_1^+-field at a plane located underneath the tip. The distance between the tip and shaft is short enough (~30 mm) relative to the wavelength at 3T to assume a uniform incident B_1^+-field from the tip to the shaft. To acquire the B_1-map underneath the tip of the electrode on plane P1, the Siemens' product low-power pre-saturated turbo-flash B_1-mapping pulse sequence was used with TR/TE = 10 000 ms/2.24 ms, saturation pulse's nominal flip-angle (nFA) = 80°, read-out flip-angle = 5°, in-plane resolution = 1 mm, slice thickness = 3 mm, acquisition matrix = 256 × 256, no. of averages = 1, pixel bandwidth = 490 Hz/pixel, and acquisition time = 20 s. Parallel imaging using the generalized autocalibrating

partial parallel acquisition technique with the acceleration factor of 2 was performed. The outcome of this pulse sequence is a flip-angle (*FA*) map, whereas the absolute B_1^+ values are required for current measurement. Using the vendor's definition of the reference transmitter voltage, this flip-angle map in degrees can be transformed to an absolute B_1^+ per unit-volt map (μT/V) as follows:

$$\left|B1^+_{\text{per Volt}}\right| = \frac{\pi \times FA}{\gamma \times V_{\text{ref}} \times T_{\text{ref}} \times nFA}, \tag{16}$$

where γ is the gyromagnetic ratio (267.52 rad/s/μT for proton), and V_{ref} denotes the transmitter voltage required to achieve a 180° flip-angle using a 1 ms (T_{ref})-square pulse. Given the B_1^+ per unit-volt (μT/V) map corresponding to a distinct set-up, the root-mean-square (RMS) B_1^+ map in the heating study (i.e., TSE pulse sequence) with the same set-up can be calculated as follows:

$$\left|B1^+_{\text{rms}}\right| = \left|B1^+_{\text{per Volt}}\right| \times V_{\text{rms}}, \tag{17}$$

where V_{rms} represents the RMS amplitude of the RF pulse in the heating study. Given the RF pulse's envelope, *s(t)*, V_{rms} can be calculated as follows:

$$V_{\text{rms}} = \sqrt{\frac{1}{2TR}\int_0^{TR} |s(t)|^2 dt}. \tag{18}$$

Simple averaging on the B_1^+map was performed in a $30 \times 30\ \text{mm}^2$ area around the tip of the electrode (plane P1) to estimate the incident B_1^+ field. In addition, to locate the Tx-null, a low-flip-angle 3D gradient-echo (GRE) image was acquired with FA = 5°, TR/TE = 20 ms/2.64 ms, in-plane resolution = 0.5 mm, slice thickness = 3 mm, acquisition matrix = 320 × 320, no. of averages = 1, pixel bandwidth = 355 Hz/pixel, and acquisition time = 105 s on an axial plane P2 intersecting the shaft of the electrode. Using Equation (10) along with the measured incident B_1^+ and the null's location, the induced current on the shaft of the DBS electrode was calculated.

In the calibration phase, the V_{rms} as 32.4 V corresponding to the RF pulse of the TSE pulse sequence was calculated, which was used in the heating study. As shown in Figure 2C, This RF pulse was composed of a 90°-excitation pulse and a train of fifteen 150°-refocusing pulses, each 3.84 ms with echo spacing of 12.9 ms. Using the B_1 maps ($\mu T/V$) acquired, the RMS incident B_1^+ around the electrode was calculated as 1.85 μT. As shown in Figure 2D, the distance between the Tx-null and the electrode was measured as 4.9 mm, and the shaft of the electrode was aligned in the z-direction. Therefore, both θ_r and φ_r were 0, and the induced current on the electrode was calculated as 89 mA using Equation (10).

3.4 | Quasi-static EM simulations

The electro quasi-static (EQS) mode of a multi-physics simulator (Sim4life) was used to model the accumulated charges on contacts of the DBS electrode. As shown in Figure 2E, the model was composed of 4 perfect electric conductor (PEC) cylinders mimicking the contacts of the electrode and a lossy $150 \times 280 \times 70\ \text{mm}^3$ box with $\varepsilon_r = 79$ and $\sigma = 0.45$ S/m representing the gel phantom. The EM properties of the gel phantom were measured using a dielectric assessment kit (DAK12, SPEAG, Zurich, Switzerland). Identical Dirichlet boundary conditions were imposed with an initial electric potential value of 1 V on the 4 contacts while also assigning the 0-potential to the faces of an adequately large box defining the boundaries of the problem. The potential difference between the cylinders and the infinity box represents the contact voltage, V_c. Regarding the discretization of the problem, the meshing toolbox of the simulator was used with the "extremely fine" setting on the contacts and the "fine" setting for the rest (Figure 2F). The total number of voxels in this problem was 6.5×10^5, and the simulation time was 60 s on a workstation with 2 quad-core Intel(R) Xeon(R) W-2245 processors with a 3.9 GHz clock rate, 1 NVIDIA Quadro P2200 GPU, and 64 GB RAM.

In the calibration phase, the contact voltage, V_c, in the EQS simulation was iteratively adjusted to achieve an agreement between the simulated and measured temperature rise.

3.5 | Transient thermal simulations

The transient thermal (TT) mode of the same solver (Sim4life) was used to solve the bioheat equation by simply linking the EQS and TT simulation such that the SAR distribution obtained from the EQS simulation was used as a heat source in the TT simulation. The heat source was set to be active for the same duration of the TSE acquisition time. In the TT simulation, the contacts were modeled as copper cylinders with $\rho_m = 8960\ \text{kg/m}^3$, $c_p = 385$ J/kg/°C, $\kappa = 386$ W/m/°C, $\mu = 0$, and the thermal properties of the gel were assigned as $\rho_m = 1030\ \text{kg/m}^3$, $c_p = 4250$ J/kg/°C, $\kappa = 0.583$ W/m/°C, $\mu = 0$, as measured with KD2 Pro thermal properties analyzer (Decagon Devices, Pullman, WA). Regarding the discretization, the solver's meshing toolbox with the "fine" setting was used for the entire problem region (Figure 2G). The total number of voxels turned out to be 1.5×10^5, and the simulation time was 12 min on the same workstation. The TT simulation resulted in a time-varying temperature distribution in the phantom.

In the calibration phase, the time course of the simulated temperature increase close to the contact C1 was

plotted at the same location (~2.5 mm) where the temperature probe in the heating study was placed. The V_c was iteratively adjusted to match the numerically calculated and experimentally measured temperature rise. The final value of the contact voltage, 7.85 V, along with the measured value of the shaft current, 89 mA, determined the transimpedance of this particular DBS electrode to be 88 Ω. Note that in this manuscript, the V_c values are calculated and presented in the RMS form to match the measured RMS currents. However, some simulation software uses peak amplitude form.

3.6 | Experimental validation

To validate the calculated transimpedance and also to demonstrate the temperature prediction with the proposed workflow (second phase), several heating experiments were conducted. Inducing RF heating with TSE pulse sequences, temperature prediction around different contacts of the electrode with different trajectories and terminations were explored. In each experiment, the 3 steps of temperature prediction were followed as detailed in the second phase of the workflow: MR-based current measurement of I_s, EQS simulation by assigning $V_c = I_s \times R_{DBS}$, and TT simulation. The temperature is experimentally measured using temperature probes and compared to numerically predicted temperature increase. The comparison between the experimentally measured and numerically predicted temperatures was quantified using 2 error measures: normalized-root-mean-squared error (NRMSE) and peak temperature-increase error (pTIE).

3.6.1 | Different trajectories

In the first set of heating studies, 10 cases were investigated by altering the lead trajectories, RF excitation patterns (i.e., quadrature and linear excitation of the body coil), input power level, and the orientation of the shaft (i.e., oblique lead). The first case with trajectory 1, as shown in Figure 3A, was exposed to a quadrature excitation and used in the calibration phase. In the second case, the same trajectory was exposed to a linear excitation (i.e., linear excitation refers to channel 1-only excitation through this manuscript), and the temperature increase was predicted following the second phase of the proposed workflow. Similarly, cases 3 through 8 correspond to trajectories 2 to 4 (Figure 3B-D) exposed to quadrature and linear excitations. A TSE pulse sequence with the same parameters presented in Section 3.2 was used to heat the implant in cases 1 through 8. In case 9, trajectory 4 was exposed to the linear excitation similar to case 8 but with a higher input power level (i.e., the input power was increased from 20 to 30 W by decreasing the TR of the TSE pulse sequence from 300 to 203 ms). In case 10, trajectory 5 (Figure 3E) corresponding to an oblique lead (i.e., $\theta_r = 22°$, $\varphi_r = 0$) was exposed to the linear excitation similar to case 8 with the same input power level.

3.6.2 | Different terminations

In the second set, the heating experiment with 5 different set-ups were conducted by altering the termination of the DBS electrode (e.g., open, extension cable, and IPG) and the RF excitation pattern. In case 1, the electrode with a trajectory shown in Figure 4A was exposed to a linear excitation. In cases 2 and 3, quadrature and linear excitations were, respectively, applied to the DBS electrode with an extension lead (see Figure 4B). In case 4, the trajectory of the extension lead was altered (Figure 4C) and exposed to the quadrature excitation. In case **5**, a commercial IPG (Infinity DBS system, Abbott Laboratories, Chicago, IL) was connected to the extension cable (Figure 4D) and exposed to a quadrature excitation. The IPG was set into

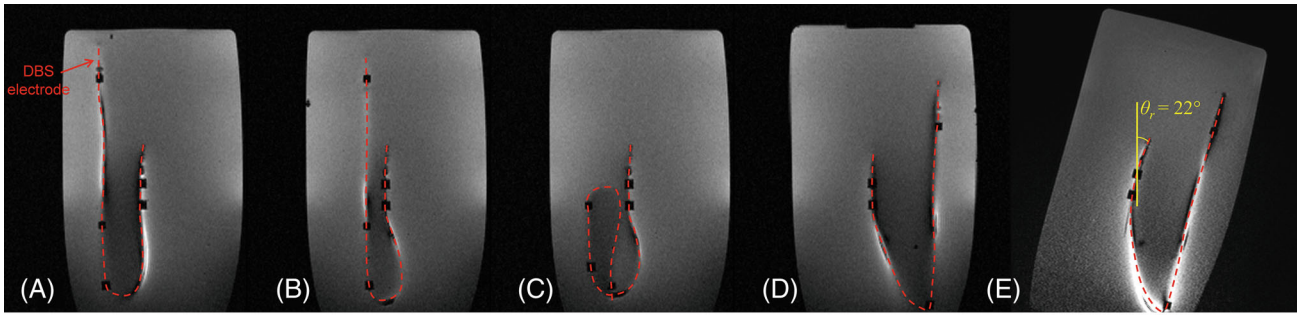

FIGURE 3 Trajectories of the deep brain stimulation (DBS) electrode used in the set of "different trajectories" studies as a part of the validation experiments. (A) Trajectory 1 was used in the calibration phase. (B) Trajectory 2, (C) trajectory 3, and (D) trajectory 4. (E) Trajectory 5, the phantom was tilted on the coronal plane, so the electrode was oblique to the axial plane and had a 22° angle with the main magnetic field B_0

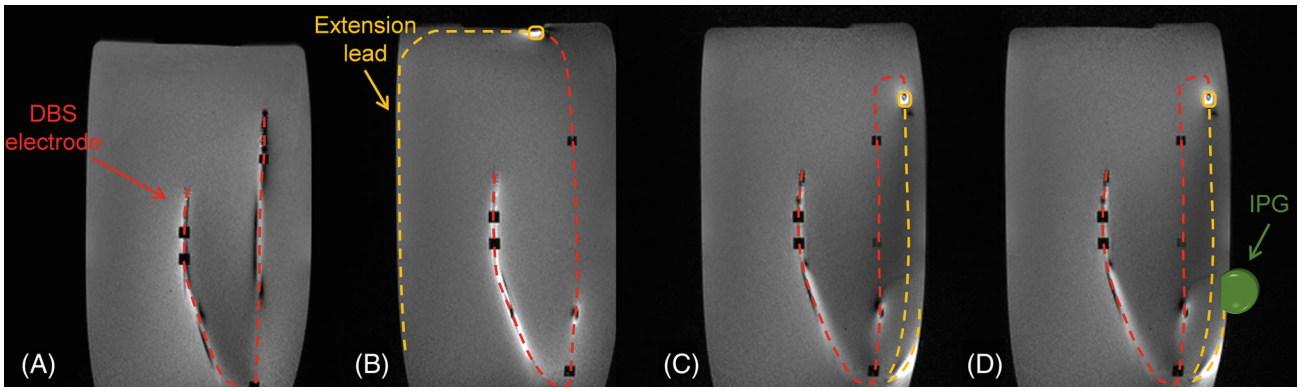

FIGURE 4 Trajectories of the deep brain stimulation (DBS) electrode used in the set of "different terminations" studies as a part of the validation experiments. (A) The DBS electrode with an arbitrary trajectory. (B) The DBS electrode was connected to the extension cable. (C) The trajectory of the extension cable was altered. (D) A commercial IPG was connected to the extension cable

FIGURE 5 Arrangement of the deep brain stimulation (DBS) electrode and temperature probes used in the set of "different contacts" studies as a part of the validation experiments. (A) The trajectory of the electrode. (B) Arrangement of the temperature probes

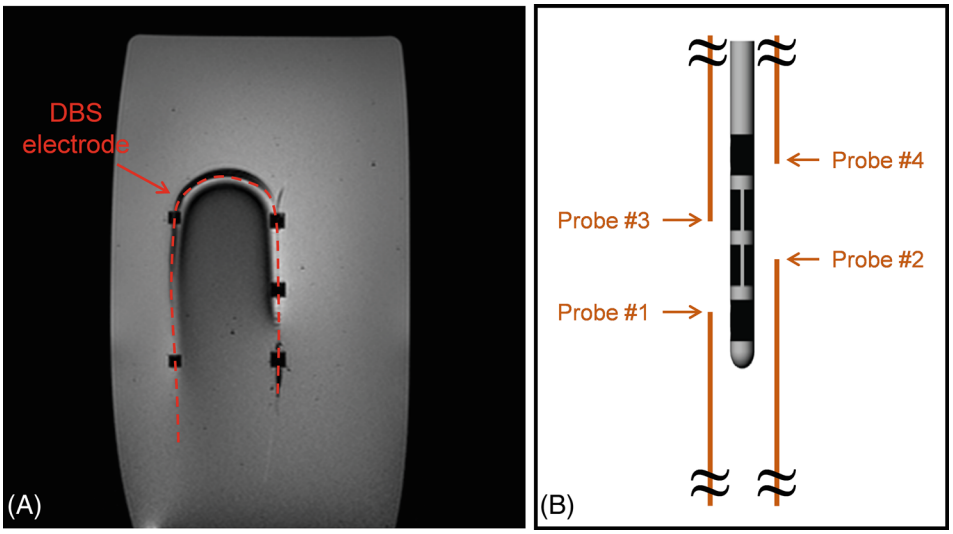

the MR mode before the experiment (i.e., no stimulation was applied during the MRI scan).

3.6.3 | Different contacts

In the third study, the validity of the proposed model for predicting the temperature increase around different contacts was investigated. For this purpose, 4 temperature probes were placed in close proximity to each contact and conducted a heating experiment with the DBS electrode whose trajectory is shown in Figure 5A, exposed to a quadrature excitation. The location of the probes with respect to the electrode is shown in Figure 5B.

3.6.4 | Different distances

The last set of studies was designed to investigate the spatial distribution of the temperature increase around a DBS electrode with an extension lead and to compare the outcomes of the simulation model with the experimental measurement. For this purpose, 4 temperature probes were placed at different radial distances around the contact C4 and conducted 2 heating experiments with the same lead trajectories (Figure 6) but different power levels of a quadrature excitation (level 1: 22.8 W; level 2: 37.8 W).

4 | RESULTS

4.1 | Experimental validation

The induced RF currents on the shaft of the DBS electrode were calculated for each case using the technique presented in the theory and methods sections.

4.2 | Different Trajectories

Figure 7A shows the experimentally measured and numerically simulated temperature increase around the

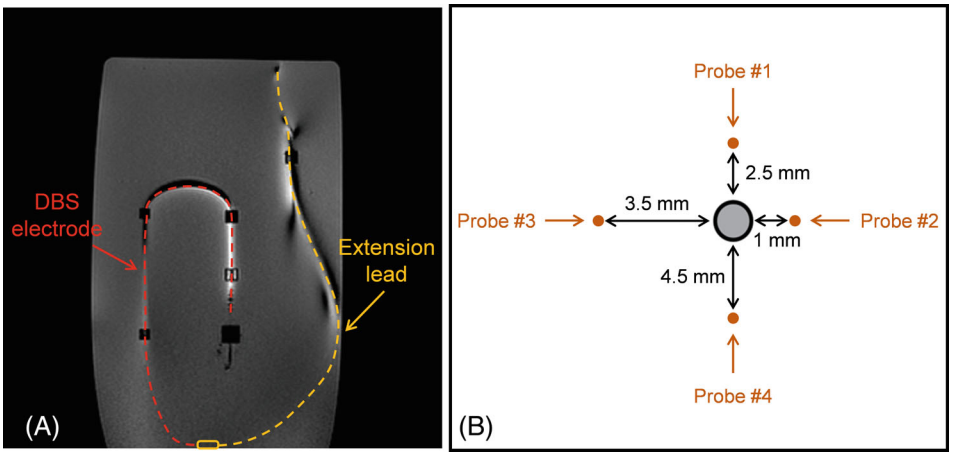

FIGURE 6 Arrangement of the deep brain stimulation (DBS) electrode and temperature probes used in the set of "different distances" studies as a part of the validation experiments. (A) The trajectory of the DBS electrode and the extension cable. (B) Positions of the temperature probes around the electrode

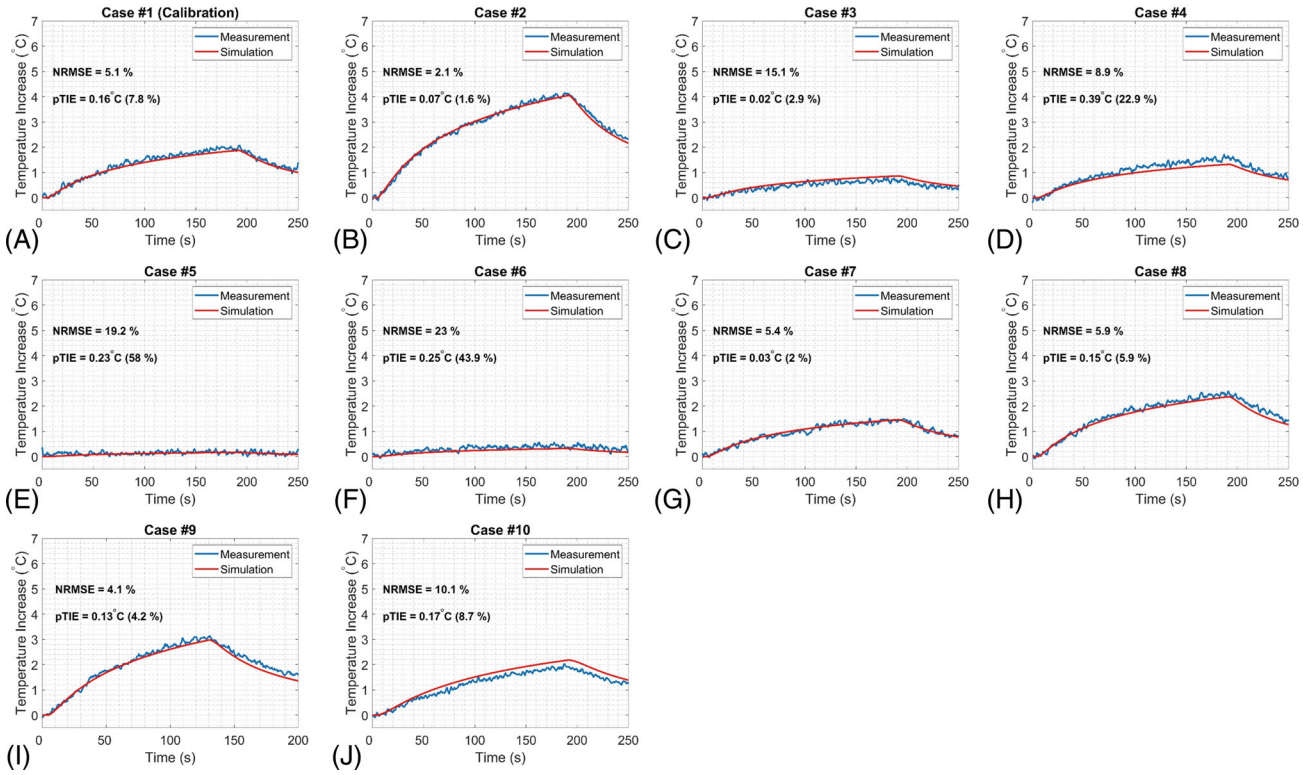

FIGURE 7 Comparisons between the experimentally measured and numerically calculated temperature increase in the set of "different trajectories" studies. (A) Case 1 was used in the calibration phase, and (B-J) cases 2 through 10 were used for validation purpose (see Figure 3 for trajectories)

contact C1, corresponding to the calibration case. As presented in Figure 7A, the calibration was performed by matching the simulated temperature increase to the experimental 1 with 5.1% NRMSE. Similarly, Figure 7B-J presents a comparison between the predicted and measured temperature increase around the same contact for 9 different trajectories (Figure 3) and RF excitation patterns. The proposed technique has accomplished the temperature prediction task for all cases with <23% NRMSE.

4.2.1 | Different terminations

Figure 8A-E shows results from the comparison between simulated and measured temperature increase around the

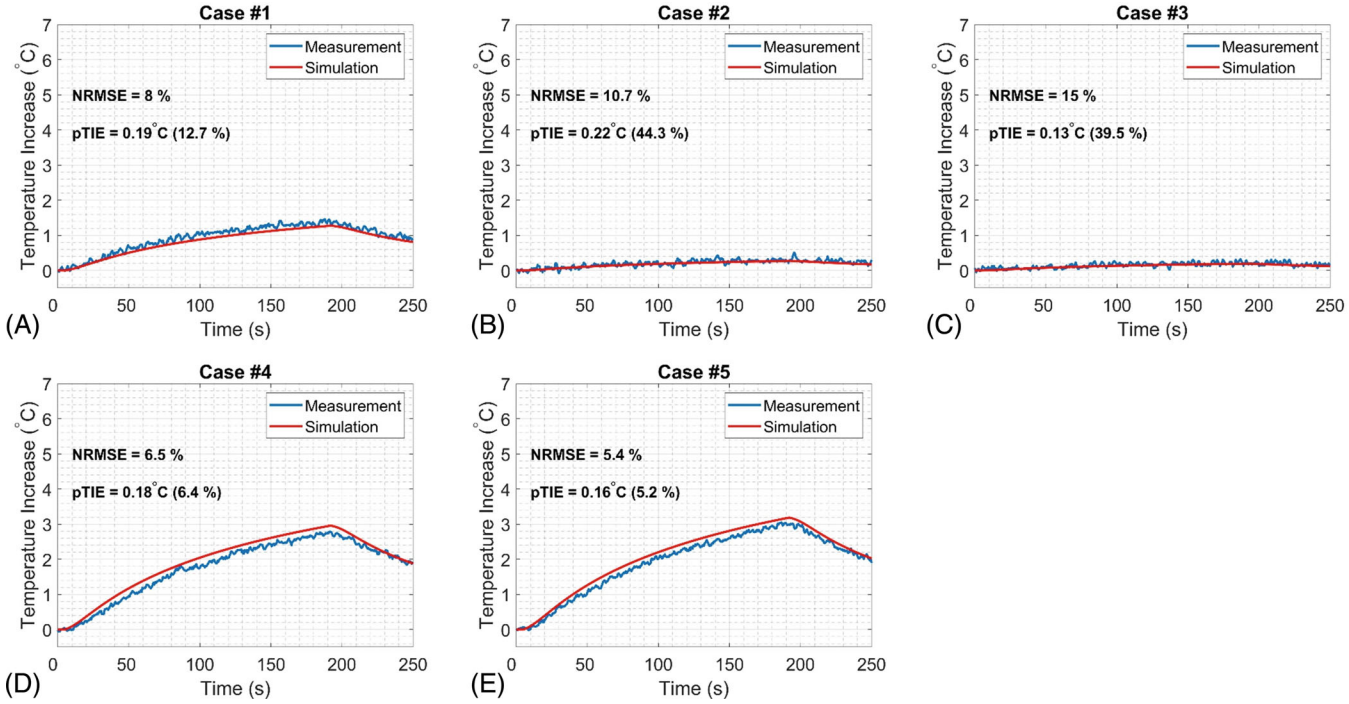

FIGURE 8 Comparisons between the experimentally measured and numerically calculated temperature increase in the set of "different terminations" studies. (A) The electrode with a trajectory shown in Figure 4A was exposed to a linear excitation. (B-C) Quadrature and linear excitations were respectively applied to the deep brain stimulation (DBS) electrode with an extension lead (see Figure 4B). (D) The trajectory of the extension lead was altered (Figure 4C) and exposed to the quadrature excitation. (E) A commercial IPG was connected to the extension cable (Figure 4D) and exposed to a quadrature excitation

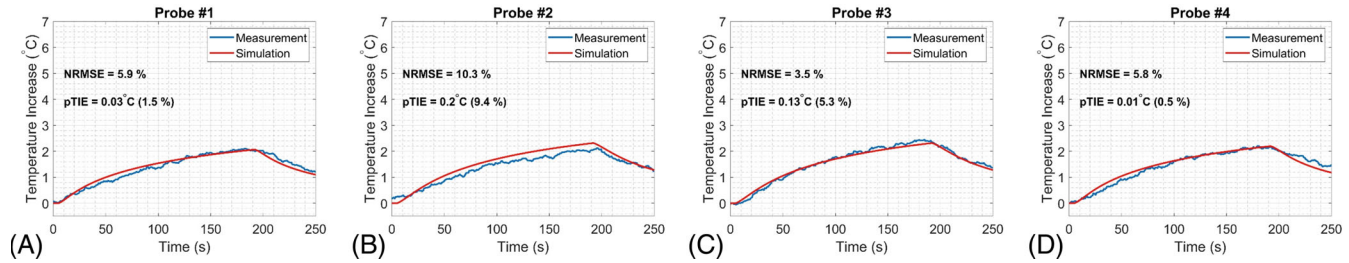

FIGURE 9 Comparisons between the experimentally measured and numerically calculated temperature increase in the set of "different contacts" studies (Figure 5). (A-D) Temperature increases were recorded at 4 different locations in the proximity of each contact

contact C1 while altering the DBS electrode termination, and RF excitation pattern. The worst temperature prediction case among these 5 cases has resulted in 15% NRMSE.

4.2.2 | Different contacts

Similarly, Figure 9A-D supports the accuracy of the temperature prediction workflow for all contacts (i.e., C1-C4) by presenting a comparison between the simulated and measured temperature increase around different contacts. The temperature increase around all contacts has been predicted by a <10.3% NRMSE.

4.2.3 | Different distances

Furthermore, as shown in Figure 10A-H, the accuracy of the simulation model has been tested by measuring the temperature increase at different radial distances around one of the contacts (i.e., C4) with 2 different RF exposure power levels. The model has predicted the temperature rise at all distances with a <10.7% NRMSE.

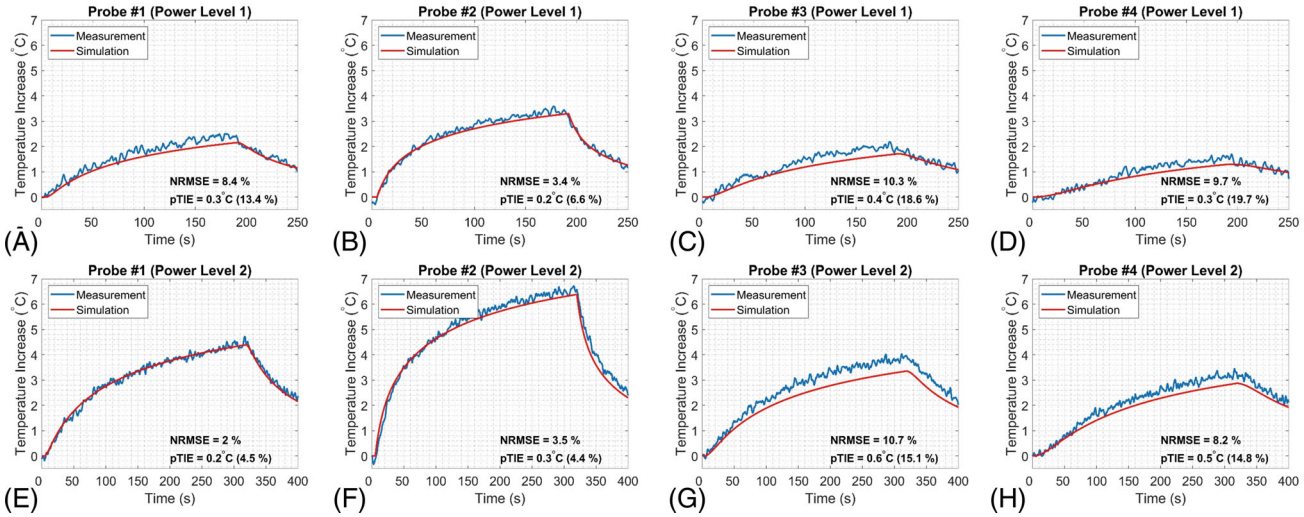

FIGURE 10 Comparisons between the experimentally measured and numerically calculated temperature increase in the set of "different distances" studies (Figure 6). Temperature increases were recorded at 4 different radial distances from contact C4 while the deep brain stimulation (DBS) lead was exposed to the RF power (A-D) level 1 (22.8 W) and (E-H) level 2 (37.8 W)

5 | DISCUSSION

In this study, a workflow was proposed based on an MR-based current measurement and a simple EM/thermal simulation to predict the RF heating at the tip of a commercial DBS electrode. The accumulated electric charge on the electrode contacts was modeled as an electrical potential boundary condition on the conductive contacts in the EM simulation environment. Hence, to relate the measured induced RF current on the electrode to this electric potential, an equivalent transmipedance R_{DBS} was defined specific to the DBS electrode and its value was calculated for a commercial DBS electrode (directional lead, Infinity DBS system, Abbott Laboratories). Furthermore, using the calculated transimpedance and EM/thermal simulations, temperature increases for different excitation conditions and lead trajectories were accurately predicted. Note that the proposed transimpedance R_{DBS} is different from the equivalent impedance seen by the IPG. The latter is an impedance between the electrode and ground, whereas the R_{DBS} is defined to relate the contact voltage to shaft current.

Our workflow can be used to predict the temperature increase at the contacts of an electrode, which are known to heat hazardously under RF exposure. It is noteworthy that this approach neither predicts any possible temperature increases around the IPG nor suggests neglecting it. In contrast, the temperature increase around IPGs, which is often ignored in the literature, should be investigated thoroughly in a different study.

In this work, an identical voltage boundary condition (V_c) was assigned to all contacts in the EM simulation environment, resulting in a single transimpedance for the electrode. Although this model is sufficient to predict the temperature increase around contacts of the electrode under investigation, defining different voltage boundary conditions on the contacts is possible, in principle. In such a case, where different voltage boundary conditions dictate different transimpedance for each contact, our strategy would still be valid to determine the transimpedance values.

The closed-form expression was expanded to determine the induced current on an obliquely oriented DBS lead, which was originally calculated by Eryaman et al[22] for a lead perpendicular to the transverse plane. The patient-safe pre-scan current measurement technique[22] used in this work is based on a low-power turbo-flash B_1-mapping and low-flip-angle GRE pulse sequences with a total acquisition time of 105 and 20 s, respectively. This technique provides a shorter pre-scan duration compared to the technique that was previously proposed by van den Bosch et al[26] (acquisition time: 124-323 s) and comparable duration to Griffin et al's technique[27] (acquisition time: ~55 s).

Our proposed temperature prediction method uses an offline calculated transimpedance along with a simple EM/thermal simulation. Therefore, it does not require real-time temperature monitoring or any modification on the DBS hardware,[21] which could be challenging from the vendors' perspective. Furthermore, it was hypothesized that the calculated transimpedance is independent of the electrode trajectory and RF excitation pattern. Therefore, our calculations do not require any complex modeling efforts[9,10] to simulate the full DBS model

within the transmit coil[11,12] and measure the incident field for computing the transfer matrix.[19,20] This hypothesis was experimentally validated by exposing the electrode to arbitrary incident fields generated by the body coil of a 3T Siemens MR scanner (MAGNETOM Prisma, Siemens Healthineers). However, because this is a patient safety problem, researchers are strongly encouraged to run additional studies with their own hardware before using the proposed workflow in imaging actual human subjects.

To validate our proposed formulation for calculating the induced current on an oblique DBS lead (Equation [10]), a DBS lead was immersed in a box-shaped phantom at an angle of 22° with respect to the main magnetic field B_0 (Figure 3E). It is noteworthy that the examined angle is merely a proof-of-concept case and does not necessarily reflect a realistic polar angle for in vivo targets. To further investigate the effect of this angle, a DBS lead with a 45° polar angle in a head-shaped phantom was also investigated. The results presented in Supporting Information Figure S1 show good prediction accuracy of the proposed model (<5% NRMSE) in the case of a highly tilted DBS lead.

Experimental data demonstrate that the transimpedance is independent of the electrode trajectory and termination scenario. It was also hypothesized that the transimpedance does not depend on the size/shape of the surrounding medium. To test this hypothesis, a single heating experiment was conducted with the same DBS electrode obliquely immersed in a head-shaped uniform phantom (same gel content). Furthermore, using the previously calculated R_{DBS}, the temperature was predicted at the tip of the electrode. The outcomes of this study (Supporting Information Figure S1) show that despite a significant change in size and shape of the phantom (i.e., from a box phantom to a head-shaped phantom), the same R_{DBS} value can successfully be used for temperature prediction. Although, it would be reasonable to assume that its value is dependent on the electrode model and/or contact geometry as well as the EM properties of the medium surrounding the contacts. These dependencies were not studied in this work. On the other hand, for a given electrode, the experiments can always be conducted by using a gel with EM properties approximately matching the EM properties of the human tissue. By doing so, one could use the transimpedance value to predict the RF heating behavior of the electrode in a perfusion-free tissue, which constitutes a thermally worst-case heating scenario. Therefore, in principle, the proposed approach can be used to predict the worst-case heating scenario for in vivo experiments. The validity of the later hypothesis should be investigated with in vivo animal and/or human cadaver studies.

Based on Equation (10), the incident B_1^+ field around the shaft needs to be known to calculate the induced current on the shaft of the electrode. In general, calculating the incident field from the scattered field around the shaft of the electrode is a complex problem. Because the distance between the tip and shaft of the electrode (~30 mm) is much smaller than the EM wavelengths inside the human body at 3T (~300 mm), it is assumed that the incident field around the shaft is approximately equal to the incident field at the tip. To verify this assumption, flip-angle maps on 2 axial planes 30 mm apart were acquired (i.e., planes P1 and P2) in the uniform box-shaped phantom without the DBS electrode. As shown in Supporting Information Figure S2, the average flip-angle, and so the B_1^+, within the indicated ROI alters by <1%. Note that this assumption is valid for the 3T DBS imaging problem and targets close to the middle of the brain where the incident field can be assumed uniform. However, for higher field strengths and/or implants located at different human body parts, other current measurement techniques[26–28] may be more accurate.

MR-based current measurement used in this work may be prone to error mainly because of the limited resolution/SNR of the low-flip-angle GRE image. Based on Equation (10), the induced current on the shaft is linearly related to the Tx-null's distance from the electrode. Hence, an error, ε, in Tx-null's measurement also leads to an error in the current measurement. For example, a Tx-null distance measured as $(1 \pm \varepsilon)$-fold the actual distance, the current would be measured incorrectly as $(1 \pm \varepsilon)$-fold the actual current. Given that the SAR quadratically changes with the shaft current, the above described underestimation would lead to $|\varepsilon^2 - 2\varepsilon|$ underestimation in the temperature increase (i.e., $[1 - |\varepsilon^2 - 2\varepsilon|]$-fold of the actual temperature increase). The researchers who would like to apply the proposed workflow to in vivo human imaging must take into account all uncertainties that might impact the temperature prediction, including the one mentioned briefly above.

In this study, the time course of experimentally measured temperature was used to determine the value of DBS transimpedance. However, this measurement significantly depends on the radial distance of the temperature probe's tip from the electrode contacts. Therefore, it is important to accurately determine the location of the temperature probe to ensure that the simulation model matches the experimental set-up. For this purpose, the distance was initially measured using a Vernier caliper. Additionally, in the TT simulation, the distance was fine-tuned by matching the cool-down curvature of the measured and simulated temperature time course. For the cool-down period (i.e., RF exposure turned OFF), Equation (14) is reduced to a first-order homogenous linear differential

equation whose solution can be expressed as an exponentially decaying function with respect to time. In addition to medium parameters, the temperature decay also depends on the point-of-interest where the temperature is observed. This relationship is exploited to fine-tune the location of the probe in our simulation model, resulting in the best possible match between simulated and experimentally measured temperature during the cool-down period.

6 | CONCLUSIONS

A workflow was proposed for predicting the RF heating around DBS electrodes. In this workflow, the parameter DBS transimpedance, R_{DBS}, was defined that relates the experimentally measured induced current on the electrode to a voltage value used in an EM/thermal simulation model for temperature prediction. The R_{DBS} value for a commercial DBS electrode (directional lead, Infinity DBS system, Abbott Laboratories) was determined as 88 Ω, which was experimentally validated in several heating studies. The proposed technique was able to predict temperature increases around the contacts of the electrode with <23% (on average 11.3%) error.

ACKNOWLEDGMENTS

This study was supported by the following grants: NIBIB P41 EB027061, NINDS R01NS115180. The devices were donated by Abbott Neuromodulation. The authors thank Dr. Gregory J. Metzger for his constructive criticism of the manuscript.

FUNDING INFORMATION

National Institute of Biomedical Imaging and Bioengineering, Grant/Award Number: NIBIB P41 EB027061; National Institute of Neurological Disorders and Stroke, Grant/Award Number: NINDS R01NS115180

ORCID

Alireza Sadeghi-Tarakameh https://orcid.org/0000-0001-5718-6553
Xiaoxuan He https://orcid.org/0000-0003-0885-912X
Ergin Atalar https://orcid.org/0000-0002-6874-6103

REFERENCES

1. Limousin P, Pollak P, Benazzouz A, et al. Effect on parkinsonian signs and symptoms of bilateral subthalamic nucleus stimulation. *Lancet*. 1995;345:91-95.
2. Krack P, Batir A, Van Blercom N, et al. Five-year follow-up of bilateral stimulation of the subthalamic nucleus in advanced Parkinson's disease. *N Engl J Med*. 2003;349:1925-1934.
3. Benabid AL, Pollak P, Gao D, et al. Chronic electrical stimulation of the ventralis intermedius nucleus of the thalamus as a treatment of movement disorders. *J Neurosurg*. 1996;84:203-214.
4. Deep-Brain Stimulation for Parkinson's Disease Study Group. Deep-brain stimulation of the subthalamic nucleus or the pars interna of the globus pallidus in Parkinson's disease. *N Engl J Med*. 2001;345:956-963.
5. Herrington TM, Cheng JJ, Eskandar EN. Mechanisms of deep brain stimulation. *J Neurophysiol*. 2016;115:19-38.
6. Starr PA, Turner RS, Rau G, et al. Microelectrode-guided implantation of deep brain stimulators into the globus pallidus internus for dystonia: techniques, electrode locations, and outcomes. *J Neurosurg*. 2006;104:488-501.
7. Henderson JM, Tkach J, Phillips M, Baker K, Shellock FG, Rezai AR. Permanent neurological deficit related to magnetic resonance imaging in a patient with implanted deep brain stimulation electrodes for Parkinson's disease: case report. *Neurosurgery*. 2005;57:E1063.
8. Erhardt JB, Fuhrer E, Gruschke OG, et al. Should patients with brain implants undergo MRI? *J Neural Eng*. 2018;15:041002.
9. Guerin B, Serano P, Iacono MI, et al. Realistic modeling of deep brain stimulation implants for electromagnetic MRI safety studies. *Phys Med Biol*. 2018;63:095015.
10. Guerin B, Iacono MI, Davids M, Dougherty D, Angelone LM, Wald LL. The 'virtual DBS population': five realistic computational models of deep brain stimulation patients for electromagnetic MR safety studies. *Phys Med Biol*. 2019;64:035021.
11. Golestanirad L, Angelone LM, Iacono MI, Katnani H, Wald LL, Bonmassar G. Local SAR near deep brain stimulation (DBS) electrodes at 64 and 127 MHz: a simulation study of the effect of extracranial loops. *Magn Reson Med*. 2017;78:1558-1565.
12. Golestanirad L, Kirsch J, Bonmassar G, et al. RF-induced heating in tissue near bilateral DBS implants during MRI at 1.5 T and 3T: the role of surgical lead management. *Neuroimage*. 2019;184:566-576.
13. Kazemivalipour E, Bhusal B, Vu J, et al. Vertical open-bore MRI scanners generate significantly less radiofrequency heating around implanted leads: a study of deep brain stimulation implants in 1.2 T OASIS scanners versus 1.5 T horizontal systems. *Magn Reson Med*. 2021;86:1560-1572.
14. Kazemivalipour E, Keil B, Vali A, et al. Reconfigurable MRI technology for low-SAR imaging of deep brain stimulation at 3T: application in bilateral leads, fully-implanted systems, and surgically modified lead trajectories. *Neuroimage*. 2019;199:18-29.
15. Golestanirad L, Kazemivalipour E, Lampman D, et al. RF heating of deep brain stimulation implants in open-bore vertical MRI systems: a simulation study with realistic device configurations. *Magn Reson Med*. 2020;83:2284-2292.
16. Acikel V, Atalar E. Modeling of radio-frequency induced currents on lead wires during MR imaging using a modified transmission line method. *Med Phys*. 2011;38:6623-6632.
17. Park SM, Kamondetdacha R, Nyenhuis JA. Calculation of MRI-induced heating of an implanted medical lead wire with an electric field transfer function. *J Magn Reson Imaging*. 2007;26:1278-1285.
18. Zastrow E, Capstick M, Cabot E, Kuster N. Piece-wise excitation system for the characterization of local RF-induced heating of AIMD during MR exposure. In 2014 International Symposium on Electromagnetic Compatibility, Tokyo, Japan, 2014: 241–244. IEEE.

19. Tokaya JP, Raaijmakers AJE, Luijten PR, Bakker JF, van den Berg CAT. MRI-based transfer function determination for the assessment of implant safety. *Magn Reson Med*. 2017;78:2449-2459.
20. Tokaya JP, Raaijmakers AJE, Luijten PR, van den Berg CAT. MRI-based, wireless determination of the transfer function of a linear implant: introduction of the transfer matrix. *Magn Reson Med*. 2018;80:2771-2784.
21. Silemek B, Acikel V, Oto C, et al. A temperature sensor implant for active implantable medical devices for in vivo subacute heating tests under MRI. *Magn Reson Med*. 2018;79:2824-2832.
22. Eryaman Y, Kobayashi N, Moen S, et al. A simple geometric analysis method for measuring and mitigating RF induced currents on deep brain stimulation leads by multichannel transmission/reception. *Neuroimage*. 2019;184:658-668.
23. Hoult DI. The principle of reciprocity in signal strength calculations—a mathematical guide. *Concepts Magn Reson*. 2000;12:173-187.
24. Kopanoglu E, Erturk VB, Atalar E. Analytic expressions for the ultimate intrinsic signal-to-noise ratio and ultimate intrinsic specific absorption rate in MRI. *Magn Reson Med*. 2011;66:846-858.
25. Gao B, Langer S, Corry PM. Application of the time-dependent Green's function and Fourier transforms to the solution of the bioheat equation. *Int J Hyperthermia*. 1995;11:267-285.
26. van den Bosch MR, Moerland MA, Lagendijk JJW, Bartels LW, van den Berg CAT. New method to monitor RF safety in MRI-guided interventions based on RF induced image artefacts. *Med Phys*. 2010;37:814-821.
27. Griffin GH, Anderson KJT, Celik H, Wright GA. Safely assessing radiofrequency heating potential of conductive devices using image-based current measurements. *Magn Reson Med*. 2015;73:427-441.
28. Etezadi-Amoli M, Stang P, Kerr A, Pauly J, Scott G. Controlling radiofrequency-induced currents in guidewires using parallel transmit. *Magn Reson Med*. 2015;74:1790-1802.

SUPPORTING INFORMATION

Additional supporting information may be found in the online version of the article at the publisher's website.

Figure S1 Validation of the proposed workflow for an oblique DBS lead (with a 45° polar angle) implanted in a head-shaped phantom ($\varepsilon_r = 79$ and $\sigma = 0.45$ S/m). (A) A coronal view of the DBS electrode in the phantom. The temperature probe placement in the proximity of contact C1 of the DBS lead is demonstrated. (B) Depiction of the P1 and P2 axial planes that were used for incident B_1 mapping and Tx-null detection, respectively. (C) The appearance of the Tx-null and electrode in the GRE image used for the MR-based current measurement. (D) Comparisons between the experimentally measured and numerically calculated temperature increase.

Figure S2 Flip-angle maps on 2 axial planes (P1 and P2 in Figure 1C) corresponding to a quadrature excitation. The flip-angle-mapping experiment was conducted in a phantom without the DBS lead.

How to cite this article: Sadeghi-Tarakameh A, Zulkarnain NIH, He X, Atalar E, Harel N, Eryaman Y. A workflow for predicting temperature increase at the electrical contacts of deep brain stimulation electrodes undergoing MRI. *Magn Reson Med*. 2022;88:2311-2325. doi: 10.1002/mrm.29375